JOM Journal of Optical Microsystems

RESEARCH PAPER

Modeling and measurement of a miniature piezoelectric ceramic tube fiber scanner for two-photon endomicroscopy

Conghao Wang,[a] Huilan Liu,[a,b] Junjie Wang,[c] Qiang Fu,[d] Yanhui Hu,[d] Yuqian Gao,[d] Xinlei Luo,[d] Aimin Wang,[e] and Lishuang Feng[a,b,f,*]

[a]Beihang University, School of Instrumentation and Optoelectronic Engineering, Beijing, China
[b]Key Laboratory of Precision Opto-Mechatronics Technology (Ministry of Education), Beijing, China
[c]Peking University, College of Future Technology, Beijing, China
[d]Beijing Transcend Vivoscope Biotech Co., Ltd., Beijing, China
[e]Peking University, School of Electronics, State Key Laboratory of Advanced Optical Communication System and Networks, Beijing, China
[f]Hangzhou Innovation Institute of Beihang University, Laboratory of Intelligent Sensing Materials and Chip Integration Technology of Zhejiang Province, Hangzhou, China

ABSTRACT. To enable optical biopsy in clinical applications, it is essential to miniaturize fiber-optic two-photon endomicroscopy (TPEM). This study used theoretical modeling and experimental measurements on a 1-mm-outer-diameter piezoelectric ceramic tube (PZT) fiber scanner for TPEM. After determining resonant modes, the effects of the driving voltage, PZT length, PZT inner diameter, fiber cantilever length, and fiber eccentricity on the fiber's first- and second-order resonant characteristics were investigated. A 2.7-mm endomicroscopic probe was also integrated, and its two-photon imaging capability was validated using *ex-vivo* mouse heart and brain tissues. This study's findings contribute to the advancement of compact nonlinear endomicroscopy.

Keywords: piezoelectric ceramic tube fiber scanner; miniaturization; two-photon endomicroscopy; biomedical imaging

Paper 23032G received Sep. 21, 2023; revised Dec. 15, 2023; accepted Dec. 21, 2023; published Jan. 13, 2024.

1 Introduction

Endoscopic optical coherence tomography,[1,2] confocal endomicroscopy,[3–5] and two-photon endomicroscopy (TPEM)[6,7] have made significant advances, providing optical biopsy techniques with potential applications in gastrointestinal diseases. Because of its high spatiotemporal resolution, increased penetration depth, and label-free imaging of tissue organs, TPEM has received much attention.[8–10]

TPEM probes are generally divided into two scanning schemes: proximal and distal scanning.[11,12] The distal scanning scheme incorporates two- or three-dimensional scanning devices into a miniature probe, resulting in superior imaging quality and representing the prevalent implementation strategy. Microelectromechanical (MEMS) mirrors and piezoelectric ceramic tube (PZT) fiber scanners are common scanning actuators in this TPEM scheme.[13,14] Unlike MEMS mirrors, which require additional reflecting mirrors or prisms within the probe configuration for light-path deflection, the PZT-driven double-cladding fiber (DCF) scheme

*Address all correspondence to Lishuang Feng, fenglishuang@buaa.edu.cn

reduces integration challenges in miniature endomicroscopic probes. This common-path configuration makes TPEM more practical for clinical endomicroscopic applications.[15]

PZT fiber scanners' structure and electrical characteristics significantly impact the integration sizes and imaging parameters (e.g., frame rate and field of view) of miniature TPEM probes, making them critical components. Several research groups have reported the development of compact nonlinear probes with integrated outer diameters (ODs) of 2.8 mm (or even smaller).[10,16–21] However, some limitations were encountered, primarily due to the ODs of the PZT actuators and imaging objectives, which hampered further miniaturization of endomicroscopic probes.[9,13,22–24] Moreover, researchers attempting to develop miniature TPEM platforms compatible with clinical instrument channels face engineering and technical challenges as they strive to reduce probe size. A critical step in addressing this challenge is the development of PZT fiber scanners with smaller ODs (1 to 1.5 mm).

Li et al.[25] modeled and analyzed a square PZT with four piezoelectric plates with an OD of ~2 mm in 2011. They investigated its resonant modes and scanning capabilities, confirming their findings using a confocal imaging platform. Li et al.[26] expanded on the potential for raster-scanning imaging in 2012 by combining two resonant modes on the same square PZT fiber scanner. In 2019, Tekpınar et al.[27] performed modal analysis on a piezoelectric bimorph fiber scanner, confirming its suitability for Lissajous, raster, and spiral scanning. Wang et al.[28] investigated the resonant modes and scanning range of a reverse-fixed 3.2-mm-OD PZT fiber scanner designed for TPEM in 2022. However, the effects of PZT parameters on the scanning characteristics of this scanner were not discussed. Compared to square PZT and piezoelectric bimorphs, the tubular four-quadrant PZT fiber scanner remains the preferred choice. However, theoretical analyses and experimental validations for miniature tubular PZT fiber scanners remain limited.

In this study, we performed modeling and experimental measurements on a 1-mm-OD PZT fiber scanner for the TPEM platform. After extracting the scanner's resonant modes, we simulated the effects of the driving voltage, PZT length, PZT inner diameter, fiber cantilever length, and fiber eccentricity on the first- and second-order resonant characteristics in the theoretical section. We built a miniature PZT fiber scanner in the experimental section and measured its first- and second-order resonance properties. A 2.7-mm-OD TPEM probe was obtained by integrating this scanner into a lensed fiber-optic TPEM platform. The imaging capability of this probe was validated by two-photon imaging of *ex-vivo* mouse heart and brain tissues.

2 Method

2.1 Modeling and Resonant MODE Analysis of the PZT Fiber Scanner

Figure 1 shows a schematic diagram of a forward-fixed PZT fiber scanner. This scanner comprised three main parts: a PZT, a spacer, and a DCF designed for femtosecond pulses and fluorescence in a common-path configuration. The spacer was physically connected to the PZT, allowing for precise positioning of the fiber and the PZT element. Table 1 presents the detailed geometric and material parameters of the PZT, including an OD (OD_{PZT}) of 1 mm, an inner diameter (ID_{PZT}) of 0.4 mm, a length (L_{PZT}) of 8 mm, and PZT-5A as the selected material. Table 2 indicates the structural and material parameters of the built forward-fixed PZT fiber scanner, with a fiber cantilever length (L_{fiber}) of 14.3 mm.

We built the forward-fixed PZT fiber scanner using commercial software based on the finite element analysis method. The PZT geometric model was established with plane A as the reference plane, and the spacer and DCF geometric models were established with plane B as the reference plane. This device functioned as a model that combined solid mechanics and electrostatic fields. Furthermore, the four quadrants of the PZT's outer wall were defined by the driving

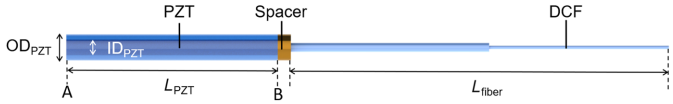

Fig. 1 A schematic diagram of the PZT fiber scanner (PZT: piezoelectric ceramic tube; DCF: double-cladding fiber).

Table 1 Parameters of the PZT mechanical structure.

PZT parameter	Value
Outer diameter (OD_{PZT})	1 mm
Inner diameter (ID_{PZT})	0.4 mm
Length (L_{PZT})	8 mm
Material	PZT-5A

Table 2 Parameters of the PZT fiber scanner mechanical structure.

Scanner parameter	Value	Scanner parameter	Value
Fiber outer cladding diameter	0.134 mm	Spacer outer diameter	1 mm
Fiber coating diameter	0.35 mm	Spacer inner diameter	0.35 mm
Fiber outer cladding length (L_{fiber})	14.3 mm	Spacer thickness	0.5 mm
Fiber coating length	8.0 mm	Spacer material	Copper

voltage conditions, the inner wall by the ground condition, and the bottom of the PZT by fixed constraints.

The PZT fiber scanner functions by driving the resonant fiber cantilever through the inverse piezoelectric effect. The scanner achieved maximum deflection at specific frequencies, denoted as resonant modes of different orders. Figures 2(a) and 2(b), respectively, illustrate the scanner's first- and second-order resonant modes, which had corresponding theoretical resonant frequencies of 799.1 and 2981.9 Hz.

2.2 Frequency Domain Analysis of the PZT Fiber Scanner

The effect of the driving voltage on the PZT fiber scanner's first- and second-order resonant characteristics was investigated using frequency domain analysis. Driving signals were applied to a single pair of PZT electrodes (e.g., $+X$ and $-X$) to ensure motion along a single axis for single-axis scanning. As shown in Fig. 3(a), the first-order frequency domain characteristics were obtained at 775 to 825 Hz frequency range (with 1 Hz increments). Meanwhile, as illustrated in

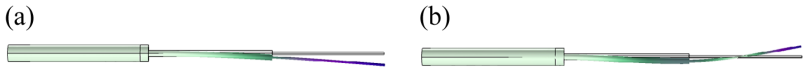

Fig. 2 PZT fiber scanner resonant mode analysis. (a) First-order resonant mode. (b) Second-order resonant mode.

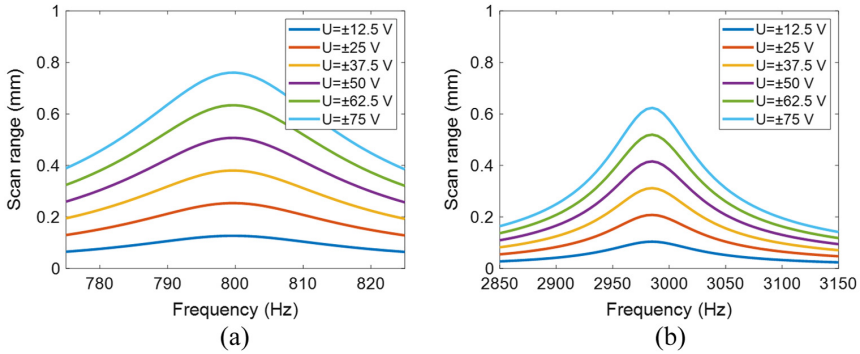

Fig. 3 Frequency domain characteristics of the PZT fiber scanner under different driving voltages. (a) First-order. (b) Second-order.

Fig. 3(b), the second-order frequency domain characteristics were at 2850 to 3150 Hz frequency range (with 5 Hz increments). Among the six simulated data groups obtained by varying the driving voltage U from ±12.5 to ±75 V with ±12.5 V increments, the first-order mode exhibited maximum scan ranges (D_1) of 0.126, 0.253, 0.379, 0.506, 0.633, and 0.76 mm. Correspondingly, the second-order mode exhibited maximum scan ranges (D_2) of 0.103, 0.206, 0.311, 0.415, 0.519, and 0.618 mm. To evaluate the PZT fiber scanner's driving capability, the driving coefficient, denoted by σ_i, was introduced. The slope of the fitted line, representing the scanner's scan range as a function of the driving voltage, was used to calculate the driving coefficient. In this case, i signifies different resonant orders. The calculated driving coefficients σ_1 and σ_2 corresponding to the first- and second-order resonant modes were determined to be 5.07 and 4.15 μm/V, respectively. According to these findings, the first-order driving coefficient σ_1 was approximately 1.22 times greater than the second-order driving coefficient σ_2 for an identical driving voltage.[25]

Following that, a systematic investigation of the PZT structural parameters, specifically the PZT length and inner diameter, was carried out to evaluate their effects on the resonant characteristics of the PZT fiber scanner. The PZT length was varied between 6 and 10 mm (in 1 mm increments). The frequency domain characteristics corresponding to the first- and second-order resonant modes are depicted in Figs. 4(a) and 4(b), respectively, under a driving voltage of ±50 V. The maximum scan ranges (D_1) of the first-order resonant mode in the context of the five datasets obtained from this parameterized analysis were 0.348, 0.424, 0.506, 0.598, and 0.696 mm. Correspondingly, the maximum scan ranges (D_2) of the second-order resonant mode were 0.225, 0.303, 0.415, 0.600, and 0.981 mm. The results showed that as the PZT length increased, the scanner's resonant frequency decreased, tending toward lower frequencies. The resonant frequencies of the scanner's first-order resonant mode were 803, 801, 800, 798, and 796 Hz. On the other hand, the resonant frequencies of the scanner's second-order resonant mode were 3010, 2995, 2985, 2950, and 2905 Hz.

Figures 5(a) and 5(b) depict the effect of the PZT inner diameter (ID_{PZT}) on the first- and second-order characteristics of the PZT fiber scanner. Five datasets were generated by increasing the PZT inner diameter from 0.1 mm to 0.3 mm (in 0.05 mm increments). Regarding the first-order resonant mode, the maximum scan ranges (D_1) of the first-order resonant mode were 0.371, 0.430, 0.506, 0.610, and 0.756 mm as the ID_{PZT} varied. Correspondingly, the maximum scan ranges (D_2) of the second-order resonant mode were 0.308, 0.354, 0.415, 0.495, and 0.611 mm. Notably, increasing ID_{PZT} decreased the thickness of the PZT tube wall, resulting in an expanded scan range for both the first- and second-order resonant modes.

Figures 6(a) and 6(b) depict the effect of fiber cantilever length on the PZT fiber scanner's first- and second-order resonant characteristics was also investigated. The initial length of the fiber cantilever, denoted as L_{fiber}, was set to 14.3 mm (shown in Table 2). A length coefficient, denoted as η, was introduced to aid in this investigation. The length of the fiber cantilever was expressed within this framework as $\eta \times L_{fiber}$. The simulated data set included five datasets obtained by increasing the length coefficient η by 0.05 increments from 0.9 to 1.1. The first-order resonant mode's maximum scan ranges (D_1) were 0.467, 0.490, 0.506, 0.520, and 0.526 mm. Meanwhile, the second-order resonant mode's maximum scan ranges (D_2) were 0.479, 0.441, 0.415, 0.395, and 0.380 mm. In this case, as the length coefficient η varied from

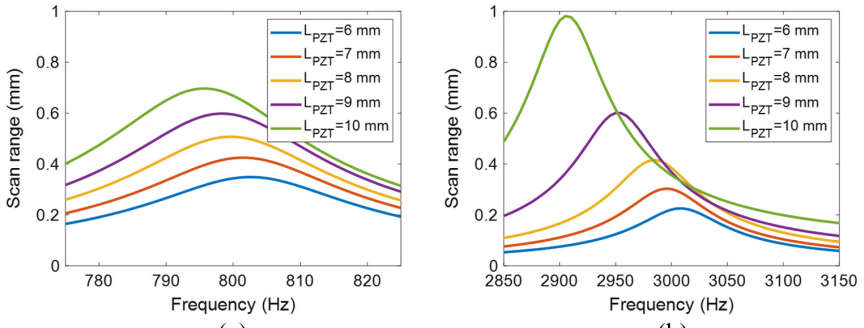

Fig. 4 Frequency domain characteristics of the PZT fiber scanner with different PZT lengths. (a) First-order. (b) Second-order.

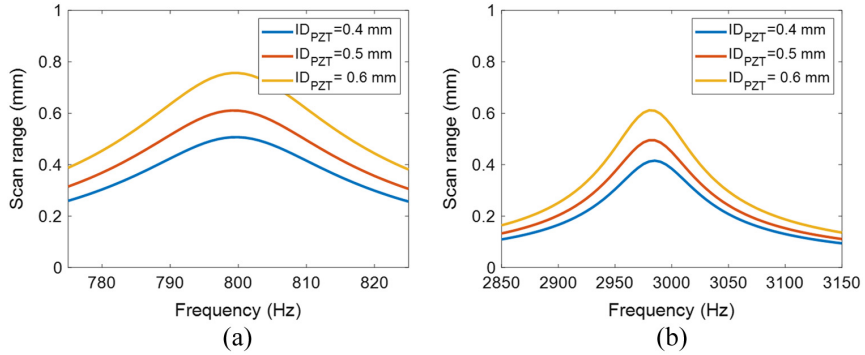

Fig. 5 Frequency domain characteristics of the scanner with different PZT inner diameters. (a) First-order. (b) Second-order.

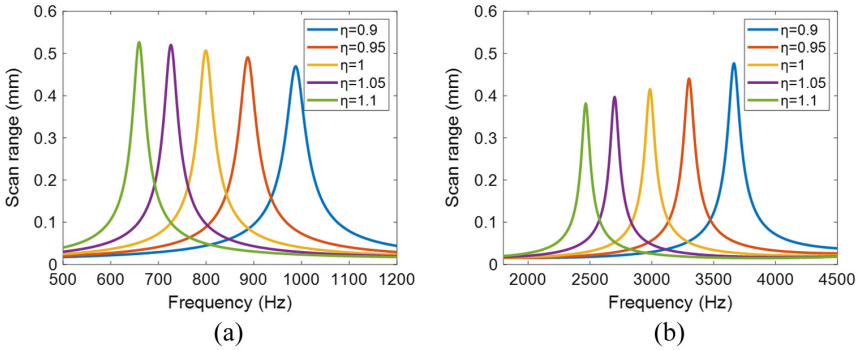

Fig. 6 Frequency domain characteristics of the scanner with different fiber cantilever lengths. (a) First-order. (b) Second-order.

0.9 to 1.1, the scanner's resonant frequency decreased, approaching lower frequencies. The resonant frequencies of the scanner's first-order resonant mode were 996, 891, 800, 723, and 654 Hz. On the other hand, the resonant frequencies of the scanner's second-order resonant mode were 3690, 3315, 2985, 2695, and 2450 Hz.

2.3 Fiber Eccentricity Impact Analysis of the PZT Fiber Scanner

The resonant characteristics of the scanner differed along the X and Y axes due to asymmetry in the fabricated PZT fiber scanner.[29] Thus, we also simulated the effect of fiber outer cladding eccentricity on resonant characteristics at various orders. Setting fiber cantilever eccentricity ($\mathrm{Dec_{fiber}}$) values at 0, 20, and 40 μm, the first-order resonant frequencies for the X- and Y-axes exhibited differences of 0.4, 5.96, and 38.14 Hz, respectively, while the second-order resonant frequencies for the X- and Y-axes exhibited corresponding differences of 1.4, 11.2, and 69.4 Hz, as depicted in Figs. 7(a) and 7(b). Apparently, non-uniformity in fiber fabrication could result in

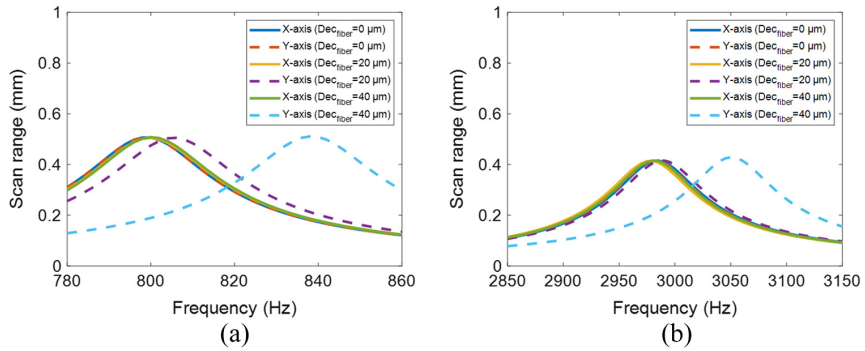

Fig. 7 Frequency domain characteristics of the scanner with different fiber eccentricity values. (a) First-order. (b) Second-order.

differences in the scanner's characteristics along the X- and Y-axes, posing challenges for image reconstruction.

3 Experiment Results

3.1 Measurement Analysis of the PZT Fiber Scanner

Using a four-quadrant tubular PZT with an OD of 1 mm, a forward-fixed PZT fiber scanner with a cantilever length of ∼14.3 mm was fabricated. Figure 8 shows a schematic representation of the static measurement platform for this PZT fiber scanner. A voltage amplifier (TD250, PiezoDrive) amplified the driving voltage signals before being applied to the tubular PZT fiber scanner via a signal generator (AFG1022, Tektronix). A CMOS camera (Panda, 4.2 M PCO) was used to record the first- and second-order resonant characteristics of the PZT fiber scanner.

Figure 9(a) illustrate the first-order resonant characteristics of a PZT fiber scanner driven by a ±50 V voltage over a frequency range of 785 to 835 Hz. Meanwhile, Fig. 9(b) depicts the voltage-scan range curves corresponding to the resonance frequency of 810 Hz. The PZT fiber scanner's first-order driving coefficients σ_1 along the X- and Y-axes were measured at 5.34 μm/V. Similarly, Fig. 9(c) depicts the scanner's second-order frequency scanning

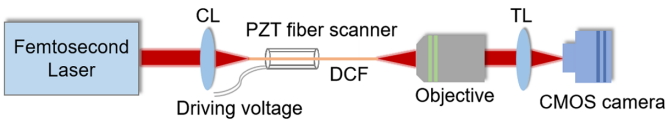

Fig. 8 A schematic diagram of the PZT fiber scanner measurement platform (CL: coupling lens, 354850 B, Lightpath. DCF: double-cladding fiber. Objective: uPlan Apo 10×, Olympus. TL: tube lens, LA1027-A, Thorlabs. CMOS camera: 4.2 M PCO, Panda).

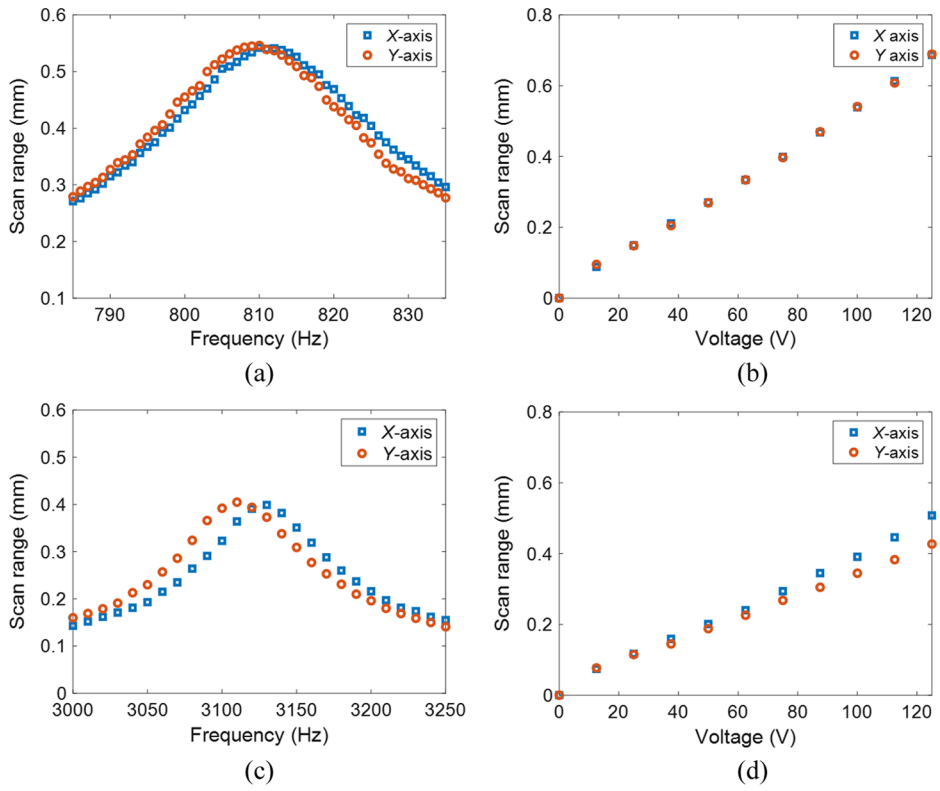

Fig. 9 Resonant characteristic results of the PZT fiber scanner. (a) Scan range versus scanning frequency curve for the first-order resonant mode. (b) Scan range versus driving voltage curve for the first-order resonant mode. (c) Scan range versus scanning frequency curve for the second-order resonant mode. (d) Scan range versus driving voltage curve for the second-order resonant mode.

characteristics in the 3000 to 3250 Hz frequency range. Consequently, Fig. 9(d) illustrates the voltage-scan range curve corresponding to the resonance frequency of 3130 Hz. The PZT fiber scanner's second-order driving coefficients σ_2 along the X- and Y-axes were measured to be 3.86 and 3.24 μm/V, respectively. These experiment results agreed with the theoretical simulation results, indicating that at the same driving voltage, the driving coefficients for the first-order resonant mode are greater than those for the second-order resonant mode.

3.2 Two-Photon Endomicroscopy Probe Integration

A common-path fiber-optic TPEM platform was developed, as shown in Fig. 10(a). The double-cladding antiresonant fiber (DC-ARF) was a delivery fiber for femtosecond pulse and fluorescence signals. The 920-nm femtosecond pulse was coupled into the core of the DC-ARF and guided to the probe's distal end. A photomultiplier tube (PMT) collected and detected two-photon-excited fluorescence signals. Previous reports contained more detailed information on the TPEM hardware platform.[30] Figure 10(b) displays the integrated TPEM probe, with an OD of 2.7 mm, a rigid length of 24 mm, and a weight of 0.33 g. Figure 10(c) depicts the schematic of the miniature TPEM probe. The lensed fiber technique aided in realizing objective-lens-free two-photon endomicroscopic imaging,[23,31,32] and detailed information on lensed fiber fabrication could be found in one Ref. 30. The lensed fiber had a working distance of ~240 μm. The PZT fiber scanner was activated by dual-channel amplitude-modulated sinusoidal and cosine voltage waveforms, allowing for a two-dimensional spiral pattern. The scanner's increased and decreased amplitude periods each had 512 turns. The scanner's increased amplitude period was used for imaging, i.e., single-side scanning, at a calculated frame rate of ~0.79 frame per second (fps). The PZT fiber scanner and lensed fiber were integrated into a three-segmented probe housing in this design, with a glass window at the end for protection.

Figure 11(a) shows the two-photon imaging results of a 380 nm fluorescent microsphere (G400 Fluoro-max, Thermo Scientific). The lateral resolution measurement results in Fig. 11(b) were obtained by extracting the horizontal intensity distribution of the microsphere and performing Gaussian fitting. This probe's measured lateral resolution was ~2.47 μm.

Figures 12(a) and 12(b) illustrate the results of two-photon endomicroscopic imaging of green-fluorescent-protein-expressing mouse *ex-vivo* heart and brain tissue, revealing the structural features of myocardial fibers and neuronal somas, respectively. In this case, the peak-to-peak driving voltages for the PZT fiber scanner along the X- and Y-axes were ±63.75 and ±56.25 V, respectively, yielding a field of view of ~440 μm. These findings supported the miniature PZT fiber scanner's suitability for the TPEM platform.

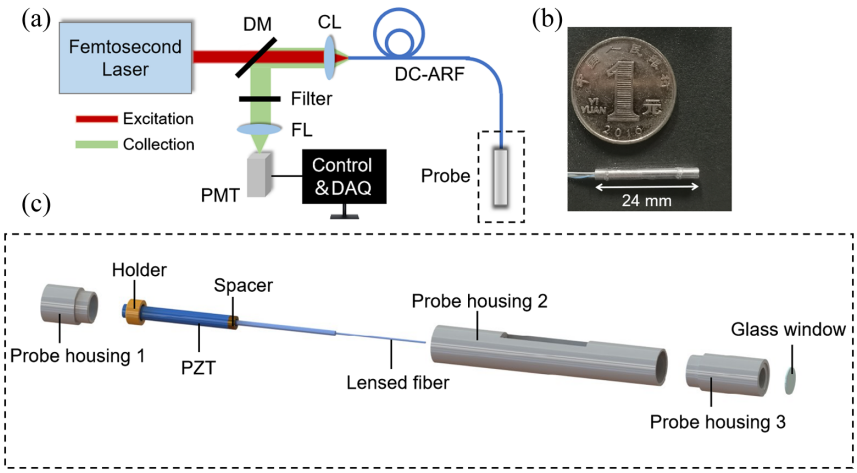

Fig. 10 Fiber-optic scanning TPEM. (a) A schematic diagram of TPEM (DM: dichroic mirror, DMLP650R, Thorlabs. CL: coupling lens, 354850 B, Lightpath. DC-ARF: double-cladding antiresonant fiber. Filter: FF01-530/43-25, Semrock. FL: focusing lens, LA1951-A, Thorlabs. PMT: photomultiplier tube, H10770PA-40-SEL, Hamamatsu). (b) Photograph of the integrated probe. (c) A schematic diagram of the integrated probe.

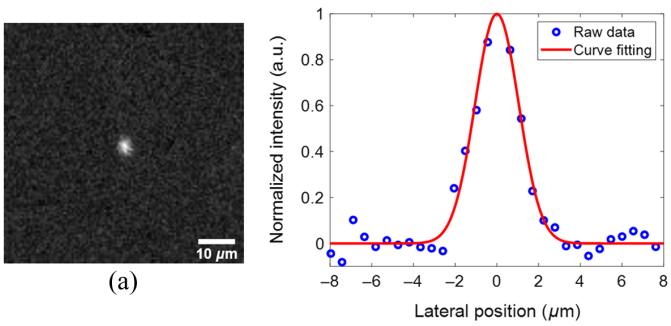

Fig. 11 (a) Two-photon imaging results of the fluorescent microsphere. (b) Lateral resolution measurement results. Blue circle: raw data. Red line: Gaussian curve fitting.

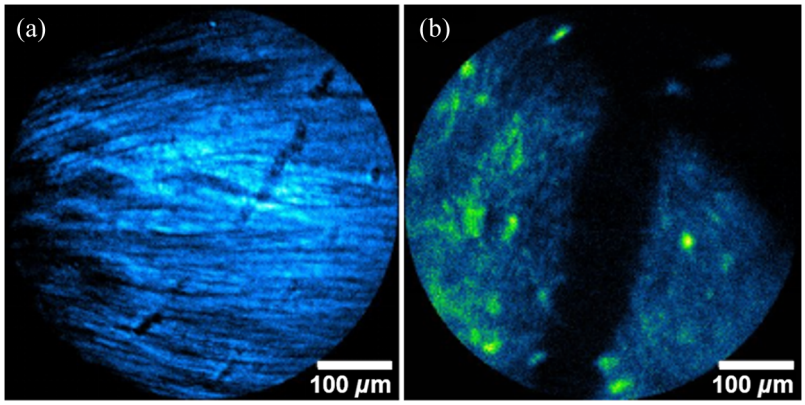

Fig. 12 *Ex-vivo* two-photon endomicroscopic imaging results. (a) Heart tissue. (b) Brain tissue.

4 Conclusion

Theoretical modeling, experimental testing, probe assembly integration, and two-photon imaging verification were performed on a 1-mm-OD PZT fiber scanner in this work. We extracted the PZT fiber scanner's resonant modes in the theoretical section. We ran simulations to determine the impact of driving voltage, PZT length, PZT inner diameter, fiber cantilever length, and fiber eccentricity on its first- and second-order resonant characteristics. We built a miniature PZT fiber scanner and measured its first- and second-order resonant characteristics in the experimental section. Furthermore, a 2.7-mm-OD lensed fiber-optic TPEM probe with two-photon imaging capability was integrated and validated using *ex-vivo* mouse heart and brain tissues. Theoretical support for the development of compact fiber-optic endomicroscopes was provided by this work. Prospectively, developing a miniature and high-speed PZT fiber scanner can broaden the application scope of multi-photon endomicroscopy techniques, especially in the dynamic recording of brain neuron activity in freely behaving animals.

Disclosures

The authors declare no conflicts of interest.

Code and Data Availability

The data underlying the results presented in this paper are not publicly available at this time but may be obtained from the authors upon reasonable request.

Acknowledgments

This research was supported by the National Key Research and Development Program of China (2020YFB1312802), National Natural Science Foundation of China (61973019, 31830036, and

61975002), and the Academic Excellence Foundation of BUAA for PhD Students. The authors thank the anonymous reviewers for their insightful and professional comments on this work.

References

1. G. J. Tearney et al., "In vivo endoscopic optical biopsy with optical coherence tomography," *Science* **276**(5321), 2037–2039 (1997).
2. M. J. Gora et al., "Endoscopic optical coherence tomography: technologies and clinical applications [Invited]," *Biomed. Opt. Express* **8**(5), 2405–2444 (2017).
3. M. Minsky, "Microscopy apparatus," US Patent 3013467 (1961).
4. J. M. Jabbour et al., "Confocal endomicroscopy: instrumentation and medical applications," *Ann. Biomed. Eng.* **40**(2), 378–397 (2012).
5. H. Li et al., "500 μm field-of-view probe-based confocal microendoscope for large-area visualization in the gastrointestinal tract," *Photonics Res.* **9**(9), 1829–1841 (2021).
6. W. Denk, J. H. Strickler, and W. W. Webb, "Two-photon laser scanning fluorescence microscopy," *Science* **248**(4951), 73–76 (1990).
7. V. Kučikas et al., "Two-photon endoscopy: state of the art and perspectives," *Mol. Imaging Biol.* **25**, 3–17 (2021).
8. W. R. Zipfel, R. M. Williams, and W. W. Webb, "Nonlinear magic: multiphoton microscopy in the biosciences," *Nat. Biotechnol.* **21**(11), 1369–1377 (2003).
9. D. R. Rivera et al., "Compact and flexible raster scanning multiphoton endoscope capable of imaging unstained tissue," *Proc. Natl. Acad. Sci. U. S. A.* **108**(43), 17598–17603 (2011).
10. W. Liang et al., "Nonlinear optical endomicroscopy for label-free functional histology in vivo," *Light Sci. Appl.* **6**(11), e17082 (2017).
11. W. Göbel et al., "Miniaturized two-photon microscope based on a flexible coherent fiber bundle and a gradient-index lens objective," *Opt. Lett.* **29**(21), 2521–2523 (2004).
12. C. M. Lee et al., "Scanning fiber endoscopy with highly flexible, 1 mm catheterscopes for wide-field, full-color imaging," *J. Biophotonics* **3**(5–6), 385–407 (2010).
13. S. Tang et al., "Design and implementation of fiber-based multiphoton endoscopy with microelectromechanical systems scanning," *Biomed. Opt. Express* **14**(3), 034005 (2010).
14. X. Duan et al., "MEMS-based multiphoton endomicroscope for repetitive imaging of mouse colon," *Biomed. Opt. Express* **6**(8), 3074–3083 (2015).
15. D. H. Hong et al., "Clinical feasibility of miniaturized Lissajous scanning confocal laser endomicroscopy for indocyanine green-enhanced brain tumor diagnosis," *Front. Oncol.* **12**, 994054 (2023).
16. M. T. Myaing, D. J. Macdonald, and X. Li, "Fiber-optic scanning two-photon fluorescence endoscope," *Opt. Lett.* **31**(8), 1076–1078 (2006).
17. Y. Zhao, H. Nakamura, and R. J. Gordon, "Development of a versatile two-photon endoscope for biological imaging," *Biomed. Opt. Express* **1**(4), 1159–1172 (2010).
18. G. Ducourthial et al., "Development of a real-time flexible multiphoton microendoscope for label-free imaging in a live animal," *Sci. Rep.* **5**(1), 18303 (2015).
19. D. Y. Kim et al., "Lissajous scanning two-photon endomicroscope for in vivo tissue imaging," *Sci. Rep.* **9**(1), 3560 (2019).
20. E. Pshenay-Severin et al., "Multimodal nonlinear endomicroscopic imaging probe using a double-core double-clad fiber and focus-combining micro-optical concept," *Light Sci. Appl.* **10**(1), 1–11 (2021).
21. H. Guan et al., "Multicolor fiber-optic two-photon endomicroscopy for brain imaging," *Opt. Lett.* **46**(5), 1093–1096 (2021).
22. Y. Wang et al., "Four-plate piezoelectric actuator driving a large-diameter special optical fiber for nonlinear optical microendoscopy," *Opt. Express* **24**(17), 19949–19960 (2016).
23. F. Akhoundi et al., "Compact fiber-based multi-photon endoscope working at 1700 nm," *Biomed. Opt. Express* **9**(5), 2326–2335 (2018).
24. A. Lombardini et al., "High-resolution multimodal flexible coherent Raman endoscope," *Light Sci. Appl.* **7**(1), 10 (2018).
25. Z. Li, Z. Yang, and L. Fu, "Scanning properties of a resonant fiber-optic piezoelectric scanner," *Rev. Sci. Instrum.* **82**(12), 123707 (2011).
26. Z. Li and L. Fu, "A resonant fiber-optic piezoelectric scanner achieves a raster pattern by combining two distinct resonances," *Rev. Sci. Instrum.* **83**(8), 086102 (2012).
27. M. Tekpınar, R. Khayatzadeh, and O. Ferhanoğlu, "Multiple-pattern generating piezoelectric fiber scanner toward endoscopic applications," *Opt. Eng.* **58**(2), 023101 (2019).
28. C. Wang et al., "Modeling and analysis of reverse-fixed piezoelectric tube fiber scanner for two-photon endomicroscopy," *Proc. SPIE* **12560**, 1256008 (2023).
29. H. C. Park et al., "High-speed fiber-optic scanning nonlinear endomicroscopy for imaging neuron dynamics in vivo," *Opt. Lett.* **45**(13) (2020).

30. C. Wang et al., "Lensed fiber-optic two-photon endomicroscopy for field-of-view enhancement," *Photonics* **10**(3), 342 (2023).
31. H. Bao and M. Gu, "A 0.4-mm-diameter probe for nonlinear optical imaging," *Opt. Express* **17**(12), 10098–10104 (2009).
32. J. B. Kim et al, "Objective-lens-free confocal endomicroscope using Lissajous scanning lensed-fiber," *J. Opt. Microsyst.* **1**(3), 034501 (2021).

Conghao Wang is a PhD candidate at the School of Instrumentation and Optoelectronic Engineering, Beihang University. His research interests include multi-photon endomicroscopic techniques.

Huilan Liu is an associate professor at the School of Instrumentation and Optoelectronic Engineering, Beihang University. Her research interests include optical sensing and MOEMS techniques.

Junjie Wang is a postdoctoral fellow at the College of Future Technology, Peking University. His research interests include multi-photon microscopic techniques.

Qiang Fu is a senior engineer at Beijing Transcend Vivoscope Biotech Co., Ltd.

Yanhui Hu is a senior engineer at Beijing Transcend Vivoscope Biotech Co., Ltd.

Yuqian Gao is a senior engineer at Beijing Transcend Vivoscope Biotech Co., Ltd.

Xinlei Luo is a senior engineer at Beijing Transcend Vivoscope Biotech Co., Ltd.

Aimin Wang is an associate professor at the School of Electronics, Peking University. His research interests include ultrafast fiber lasers and multi-photon microscopic techniques.

Lishuang Feng is a professor at the School of Instrumentation and Optoelectronic Engineering, Beihang University. Her research interests include integrated optics and MOEMS techniques.